ARTICLE

Structural and Proton Conductivity Studies of Fibrous π-$Ti_2O(PO_4)_2$·$2H_2O$: Application in Chitosan-Based Composite Membranes

Received 00th January 20xx,
Accepted 00th January 20xx

DOI: 10.1039/x0xx00000x

Artem A. Babaryk,[*a] Alaa Adawy,[b] Inés García,[c] Camino Trobajo,[d] Zakariae Amghouz,[e] Rosario M. P. Colodrero,[f] Aurelio Cabeza,[f] Pascual Olivera-Pastor,[f] Montse Bazaga-García[*f] and Lucía dos Santos-Gómez[*a]

Although the fibrous polymorphic modification of titanium phosphate, π-$Ti_2O(PO_4)_2$·$2H_2O$ (π-TiP) is known for decades, its crystal structure has remained unsolved. Herewith we report the crystal structure of π-TiP at a room temperature, determined from the synchrotron radiation powder X-ray diffraction, and corroborated by ^{31}P solid state NMR and the accurate density functional theory calculations. In contrast to the previously reported ρ-TiP polymorph, the as-synthesized hydrated phase crystallizes in the monoclinic system ($P2_1/c$, a = 5.1121(2) Å, b = 14.4921(9) Å, c = 12.0450(11), β = 115.31(1)°, Z=4) and is composed of corner-sharing titanium octahedra and phosphate units arranged in a pattern distinct of ρ-TiP polymorph. The unit cell was confirmed by SAED, while the formation of planar packing imperfections and stacking faults along the [101] was revealed by HRTEM analysis. In situ dehydration study of π-TiP, monitored by high-temperature powder X-ray diffraction, led to a new anhydrous monoclinic [$P2_1/c$, a = 5.1187(13) Å, b = 11.0600(21) Å, c = 14.4556(26), β = 107.65(2)°, Z=4) phase that crystallizes at 500°C. The latter resembles the packing fashion of the parental π-TiP, albeit titanium atoms are present both in distorted tetrahedral and octahedral coordination environments. Anhydrous π-TiP was found to partially rehydrate at room temperature adopting reversibly the structure of the initial phase. The studies carried out under different conditions of leaching and impregnation with H_3PO_4 showed that π-TiP exhibits an extrinsic proton conductivity ($1.3\cdot10^{-3}$ S·cm^{-1} at 90 °C and 95% RH) due to the presence of protonated phosphate species bounded on the particles surface, as revealed by ^{31}P MAS-NMR spectroscopy data. The composite membranes of Chitosan (CS) matrices filled with H_3PO_4-impregnated π-TiP solid show an increment of proton conductivity up to $4.5\cdot10^{-3}$ S·cm^{-1}, at 80 °C and 95% RH, 1.8-fold higher than those of bare CS membranes.

Introduction

Proton exchange membrane fuel cells (PEMFCs) are recognized as alternative to the declining alkaline fuel-cell technology and amongst key clean power sources.[1] High proton conducting materials are indispensable components required to increase the PEMFC efficiency, purposefully a wide range of membrane materials based on polymeric scaffold and hygroscopic inorganic filler (like ZrO_2,TiO_2, $TiSiO_4$, Silica etc.) have been recently reported so far.[2] For this purpose, a wide range of membrane materials incorporating hygroscopic inorganic additives into polymeric scaffolds have been recently reported.

PEMs used to have acidic groups to arrange a hydrophilic channel enabling fast proton transport. Nafion® has several superior properties such as its significant proton conductivity ($1.0\cdot10^{-1}$ S·cm^{-1}) and long recyclability without any evidence for a performance decay,[3] but its elevated fabrication costs and practical operation limitations are still major drawbacks impeding further applications. Chitosan (CS) polysaccharide-based polymeric from natural sources has a been extensively explored due to formidable film forming, excellent fuel barrier, low toxicity and low manufacturing costs.[4] Nevertheless, the main drawback of neat CS membranes is their low

[a.] Department of Physical and Analytical Chemistry, Oviedo University-CINN-CSIC, 33006-Oviedo, Spain.
[b.] Laboratory of HRTEM, Institute for Scientific and Technological Resources, University of Oviedo, 33006, Oviedo, Spain.
[c.] Nanomaterials and Nanotechnology Research Centre – CINN (CSIC), 33940 El Entrego, Asturias, Spain.
[d.] Department of Organic and Inorganic Chemistry, Oviedo University-CINN, 33006-Oviedo, Spain.
[e.] Department of Materials Science and Metallurgical Engineering, University of Oviedo, 33203, Gijón, Spain.
[f.] Universidad de Málaga, Dpto. de Química Inorgánica, Cristalografía y Mineralogía, 29071-Málaga, Spain.

Electronic Supplementary Information (ESI) available: See DOI: 10.1039/x0xx00000x

proton conductivity, which fuels up the interest to manipulate on CS scaffolds channels to facilitate proton transport.

A plausible way to optimize the proton transport carrier and enhance the PEM proton conduction is to employ amphoteric sites with proton donor/acceptor properties as proton transfer carriers, i.e. phosphoric acid,[5] ionic liquids[6] and imidazole[7]. Phosphoric acid cluster and phosphonate groups demonstrate large proton conductivity, high carrier concentration and low energy penalty for the proton transfer[8,9]. In addition, liquid phosphoric acid also shows large proton conductivity due to its structural diffusion.[10] For instance, Qin *et al*. reported a proton conductivity value of $1.09{\cdot}10^{-1}$ S·cm^{-1} without humidity for a 3D hydrogel material loaded with H_3PO_4 at 180 °C.[11] Cai *et al*. embed a sulfonated poly(ether sulfone) matrix with a mixture of phosphoric acid and cellulose nanofibers, reaching a proton conductivity of $1.54{\cdot}10^{-1}$ S·cm^{-1} at 80 °C and 100% RH.[12] Other many materials have been reported to be used as reservoir of phosphoric acid in order to enhance proton conductivity.[13-16] The direct impregnation of the polymer with the mineral acid is another alternative procedure. Kang *et al*. reviewed several post-synthetic impregnation strategies to improve the proton conductivity in PEMFCs.[17-20] For instance, Ponomareva *et al*. impregnated mesoporous metal-organic framework MIL-101 with H_3PO_4.[21] In this case, phosphoric acid did not act as ligand but enhanced the mobility of the charge carriers, providing a conductivity value of $3.0{\cdot}10^{-3}$ S·cm^{-1} at 150 °C and 0.13% RH. Thus, the incorporation of phosphate groups into the polymer matrix is an easy strategy to develop more efficient PEMs since these acid groups may supply extra hopping sites for the proton migration.

Another approach is the use of mixed matrix membranes (MMMs). Among the plethora of polymeric membrane fillers, metal phosphate (MPs) are attractive materials owing to their high proton conductivities,[22] up to 10^{-2} S·cm^{-1}, and good stability over an extended range of temperature and humidity.[23] In particular, zirconium phosphate derivatives possessing variable topologies and functionalized in different ways have been extensively studied as proton conductors.[24-27] In addition, hydrophilic channels of Nafion matrix have been also impregnated with titanium phosphate showing a high sensibility to operating humidity.[28]

On the other hand, fibrous phosphates are promising choices for their hybridization with polymers. Among these phosphates is the fibrous titanium phosphate [$Ti_2O(PO_4)_2{\cdot}2H_2O$], which crystallizes in two polymorphic forms, usually referred to as ρ- and π-TiP. The framework of ρ-TiP phase contains two channels running in parallel to the *a*-axis, where the H atoms of H_2O molecules reside. Both phases have been scarcely explored, in particular, the structure of the π-TiP phase remains still unknown. Some episodic studies have been carried out so far revealing promising broader applicability. Although ρ- and π-TiP possess limited porosity of only 11-16 m^2·g^{-1},[29] the textural properties of TiPs particles are noticeable as hierarchically porous materials.[30,31] The internal porosity can be altered by the thermally induced elimination of stoichiometric water molecules resulting in a substantial increase of nitrogen adsorption at 100–300 °C.[32] Yada *et al.* synthesized superhydrophilic thin films consisting of π-TiP micro- and nanocrystals bearing controlled morphologies.[33] In addition, TiP can be converted to superhydrophobic surfaces when modified with alkylamine molecules. Similarly, Cai *et al.* studied the formation of TiPs films on titanium substrates achieving superhydrophobicity with increasing the preparation temperature.[34] Moreover, our research group have proved the possibility of using titanium phosphates as antibacterial cement after enriching their surfaces with strontium and silver nanoparticles.[35] To our knowledge, neither electrical conductivity of those fibrous TiPs has never been explored hitherto, nor studies involving fibrous $Ti_2O(PO_4)_2{\cdot}2H_2O$ for practical application in PEMs. Employing hybrid membranes that incorporate fibrous phosphates into organic polymers could provide new seamless conduction pathways at inorganic/organic material interfaces, thus synergistically increasing the efficiency of PEMs.

In the present work we explore these possibilities. For that purpose, fibrous $Ti_2O(PO_4)_2{\cdot}2H_2O$ have been synthetized using the same procedure as previously described.[36] The atomic structure of the π-TiP polymorph is inferred from the high resolution powder X-ray diffraction. The real structure of the compound shows crystal packing imperfections as observed by high resolution transmission electron microscopy. Thermal stability and structural transformations were studied in situ using complementary high temperature powder X-ray diffraction and thermal analysis. We assembled and characterized a series of CS-based composite membranes with ^{31}P MAS-NMR spectroscopy and scanning electron microscopy. Finally, we examined the proton conductivity of the CS-based composite materials to assess to their potential application in PEMFCs.

Results and Discussion

Structure determination of π-TiP_0

Apparently, weak diffraction power of **π-TiP_0** limits significantly the structural information that can be retrieved from the measured diffraction pattern. Basic indexing was performed in a monoclinic system using the singular value decomposition (SVD) algorithm[37] and the unit cell metrics and symmetry were verified employing the Pawley fitting procedure. The crystal coordinates for initial model construction were taken from isostructurally crystallized $Ti_2F(PO_4)_2{\cdot}2H_2O$ (MIL-15) published by Serre *et al*.[38] Strong *hkl*-dependent anisotropic broadening of diffraction peaks was approximated using a spherical harmonics model.[39] Therefore, orthophosphate polyhedra were described linearly restraining P···O and O···O separations to get meaningful geometric parameters of d_{P-O} bond distances and θ_{O-P-O} bond angles, and minimize the number of independently refined parameters. The missing hydrogen atoms were attached to the corresponding oxygen atoms by referring to DFT optimized structural model, developed in the present study. A summary of the relevant crystallographic data and geometric parameters based on converged Rietveld refinement (Figure S1) are given in Table S1 and S2.

π-$Ti_2O(PO_4)_2{\cdot}2H_2O$ crystallized in the monoclinic space group $P2_1/c$, the asymmetric part of the unit cell holds whole formula unit (Z = 4). Crystalline framework of π-phase can be rationalized considering $\{(TiO_6)(PO_4)\}_2$ secondary building units (SBUs) wherein PO_4 units adopt pointing “up” or “down” respect to (Ti···P···Ti···P) base plane (Figure 1a).$\{(Ti1O_6)_2(P1O_4)(P2O_4)\}$ SBUs propagate along [001] direction connecting each other via common O6 oxygen vertices, $\{(Ti2O_6)(P1O_4)\}_2$ SBUs do the same along [010]. The angle between

(Ti1···P1···Ti1···P2) base planes (Ti2···P1···Ti2···P1) of differently oriented SBUs is 43.7°. Spatial packing arises from sharing common O3··O4 edge of $P1O_4$ tetrahedron, which belongs to $\{(Ti2O_6)(P1O_4)\}_2$, with two adjacent $\{(Ti1O_6)(P2O_4)\}_2$ units.

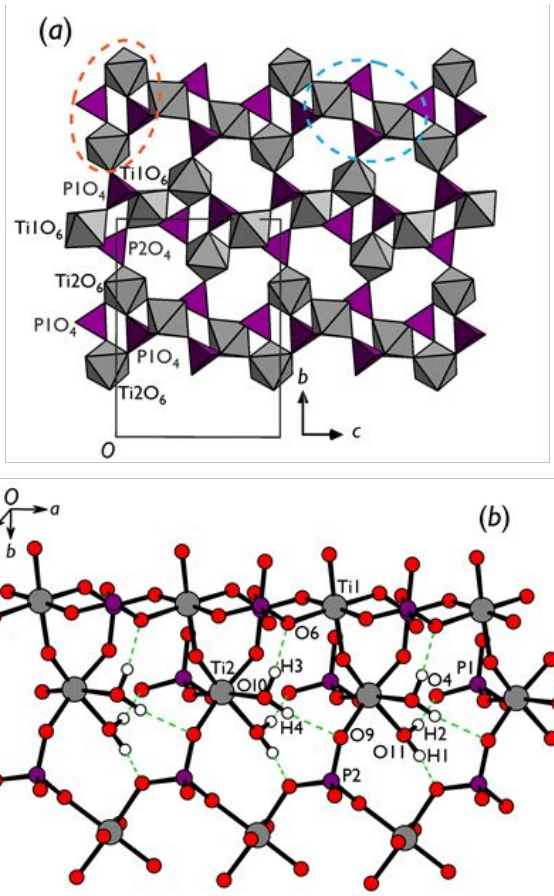

Figure 1. (a) Octahedra-tetrahedra representation of the π-TiP_0 structure projected onto (011) plane. $\{(Ti1O_6)_2(P1O_4)(P2O_4)\}$ and $\{(Ti2O_6)_2(P1O_4)_2\}$ SBUs are highlighted with orange and light blue dashed lines. (b) Best view projection of H-bonding pattern for the π-TiP_0 structure (Ti, P and O atoms are depicted as grey, maroon and red spheres, respectively).

Two water molecules exclusively belong to the coordination sphere of Ti2 and are distant from central atom at 2.170(6) ($d_{Ti2–O10}$) and 2.248(7) ($d_{Ti2–O11}$) Å, that is longer than $\langle d \rangle_{Ti–O}$ = 2.034 Å. This fact is explained by the less effective electrostatic interaction of neutral donor oxygen atoms with Ti^{+4} in comparison with those carrying negative charge within $(PO_4)^{3-}$. Terminal hydrogen atoms give a rise for a hydrogen bonding, which makes a contribution of non-covalent forces into the crystal cohesion. A pattern of two-centered O11–H1···O8, O11–H1···O9 and O11–H2···O4, O11–H2···O5 bonds bridge oxygen atoms at $\{(Ti1O_6)_2(P1O_4)(P2O_4)\}$ SBUs (Figure 1b).

On the other hand, TEM investigations showed that the **π-TiP_0** has the morphology of nanorods with an average length of ~520 nm and a diameter of ~85 nm (Figure S2a). Selected area electron diffraction (SAED) for bundles of **π-TiP_0** nanorods shows a typical ring pattern and reported some reflections consistent with those specified using PXRD (Figure S2b). An electron diffraction tomography was also performed, and its processing yielded cell parameters like those obtained by PXRD with a primitive monoclinic unit cell (a = 4.86 Å, b = 15.17 Å, c = 11.24 Å and β = 115°) (Figure 2). However, the quality of the electron diffraction tomography series was not good enough to determine the exact crystal structure due

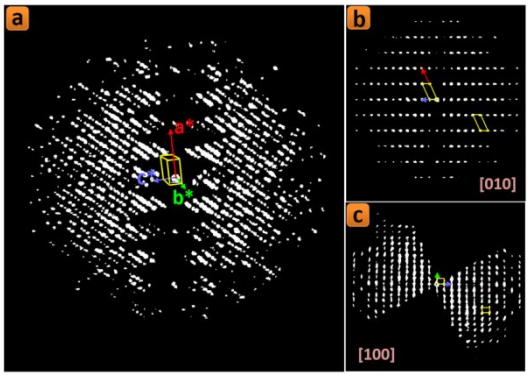

to the low crystallinity of the nanorods that resulted from the propagating defects, beside some loss of crystallinity for the nanorods during a prolonged exposure to the electron beam.

Figure 2. (a) The 3D reconstruction of the reciprocal space from an electron diffraction tilt series of a single **π-TiP_0** nanorod with ADT3D software (b) and (c) The projection of the 3D reciprocal space along the zone axes [010] and [100], respectively.

HRTEM inspection showed the lattice fringes on the **π-TiP_0** nanorods in several directions, demonstrating the crystallinity of the nanorods (Figures 4 and 5). Compared with the ρ-TiP polymorph,[32] the **π-TiP_0** generally shows less crystallinity and more crystalline defects. Although there are slight differences in the measured d_{hkl} values, most probably due to the electron beam damage, the indexing has confirmed the structural information determined relying on PXRD.

SAED and HRTEM micrographs revealed that the favorable direction of the growth for those crystalline nanorods is practically collinear to the [100] direction (Figures 4 and 5). Hence, the nanorod morphology of **π-TiP_0** is obtained as a result of the higher growth rate of the rod along the [100] compared to that along the [101] direction. According to the determined space group ($P2_1/c$), some forbidden reflections, (10–1) and (001), were observed (Figure 3

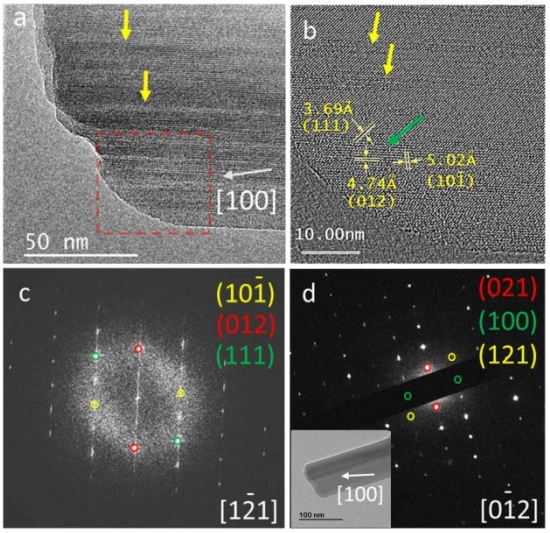

and 4). These reflections were expected to be a result of multiple elastic scattering that is usually known in electron diffraction.

Figure 3. HRTEM analysis for a nanorod of **π-TiP_0**. (a) TEM micrograph for a part of the **π-TiP_0** nanorod and the inset is its FFT. The white arrows indicate the directions [100] and [101]; (b) A magnification of the nanorod in (a) showing the crystal imperfections indicated with yellow arrows; (c) HRTEM micrograph for the area indicated by the dashed red square in (b); (d) A processed HRTEM image for the area enclosed by the dashed yellow square in (c) showing the direction of the stacking faults; (e) FFT pattern for (c) and its indexing showing the streaking of the reflection spots corresponding to plane (00−1) seen along the zone axis [010]; (f) SAED pattern of the nanorod shown in (a) taken in the same zone axis [010] showing the streaking of the diffraction spots of (001) plane.

However, in a high-resolution micrograph of a nanorod in the zone axis [010], a wave-like periodic pattern appeared in lattice fringes corresponding to the planes (10−1). Apparently, this is due to the presence of planar defects (stacking faults) altering the stacking sequence of the planes (00−1), that should be normal to (10−1) (Figure 3). These characteristic long-range stacking faults in the **π-TiP_0** nanorods also appeared as streaking in the diffraction spots corresponding to (00−1) in the fast-Fourier transform (FFT) and SAED micrographs (Figure 3e-f). The growth of the **π-TiP_0** nanorod along the [101] direction affects the atomic ordering in the (10−1) plane, in a way that forced this plane not to propagate in a straight line along its direction but rather makes, after every 6 Å distance a downward bend of ~20° that extends to 4.5 Å - length before it reverts back to the initial plane direction, resulting in a decrease in the height of the plane of around 3.0 Å in every 2 × $d_{(001)}$ spacings (Figure 3d). Several **π-TiP_0** nanorods were analyzed, and the results showed a unidirectional streaking in the spots belonging to the planes (012) seen along the zone axis [1−21], and the planes (021) seen along the zone axis [012] (Figure 4), beside that was discussed above for (001) seen along the zone axis [010] (Figure 3e-f). Noticeably, these specific planes together belong to the zone axes <100> and all of them are normal to the plane (10−1) that showed the short-range directional ordering (Figure 4a-d). This suggests that the planes (012) and (021) could have contributed in some way to this planar imperfection appeared in (10−1). This analysis also revealed that the direction [100] makes an angle of around 10° with the direction of the nanorod growth.

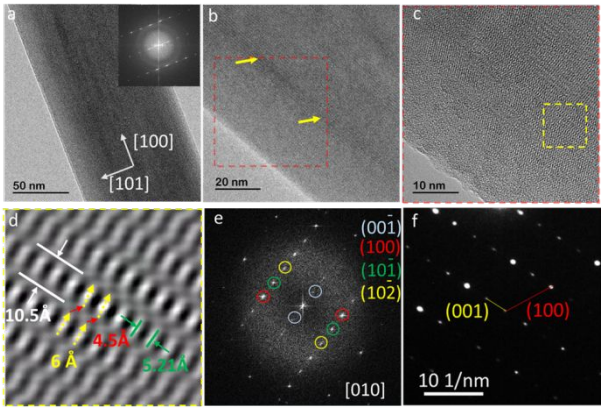

Figure 4. HRTEM analysis for two **π-TiP_0** nanorods. (a) HRTEM micrograph for part of a rod. The yellow arrows show the stacking of the (012) planes along the long axis of the nanorod. The white arrow shows the direction [100] that make an angle of less than 10° with the direction of growth of the nanorod; (b) HRTEM micrograph for the area labelled by the red dashed square in (a) showing the presence of planar defects (indicated by yellow arrows) and the only area in the view (indicated by green arrow) where details in three directions can be visualized and indexed; (c) FFT pattern of the micrograph depicted in (b) showing the streaking of the diffraction spots corresponding to (012) plane seen along the zone axis [1−21]; (d) SAED pattern for another **π-TiP_0** nanorod, shown in the inset, illustrating the streaking in the diffraction spots corresponding to the plane (021) seen along the zone axis [0−12].

Crystal structure of π-$Ti_2O(PO_4)_2$

The thermal evolution of **π-TiP_0** crystal structure was followed by HT-PXRD from room temperature up to 900 °C. As shown in Figure 5, the solid is stable until 200 °C, the temperature at which the dehydration starts. This process takes place till 400 °C and is accompanied by several consecutive structural changes. Thus, at 300 °C there is a subtle phase transition due to the partial dehydration of the solid. Its powder diffraction pattern was auto-indexed using the program DICVOL06 in a cell with parameters very close to the as-synthesized sample,[40] with the *c*-parameter doubled [*a* = 10.2815 Å, *b* = 14.3946 Å, *c* = 12.2484 Å, *β* = 114.556°, *V* = 1648.79 Å^3] in respect to π-TiP_0. This behavior was also described for $Ti^{III}Ti^{IV}F(PO_4)_2{\cdot}2H_2O$.[38] The anhydrous phase, π-$Ti_2O(PO_4)_2$, remains stable from 400 °C to 680 °C. This phase suffers a last phase transition at 680 °C to give the final decomposition products, which have been identified by PXRD pattern matching and confirmed by Rietveld analysis (Figure S3), as a mixture of TiP_2O_7 (ICSD #279581) and $Ti_5O_4(PO_4)_4$ (ICSD #59397) dominant phases.

The powder diffraction pattern of π-$Ti_2O(PO_4)_2$ at 500 °C (**π-TiP_500**) was indexed in a monoclinic unit cell with parameters *a* = 14.914(7) Å, *b* = 11.031(2) Å, *c* = 5.114(2) Å, *β*= 113.21°, *V* = 773.23 Å^3. The highest possible symmetry was assigned to $P2_1/c$ space group linking it to that of parental RT-framework. The crystal structure has been solved by simulated annealing using the crystal structure of previously reported ρ-$Ti_2O(PO_4)_2$ polymorph as an initial model[32] and refined by Rietveld method [Figure S4, Tables S3-S6]. The unit cell metrics and interatomic geometries were found in a good agreement with DFT-relaxed crystal lattice (Table S7). Thermally induced structural transformation is accompanied by departure of two water molecules [$(\Delta m/m)_{exp}$ = 10.6%, $(\Delta m/m)_{exp}$ = 10.7%, Figure S5] invoking the rebuild within of [$Ti_2O_4(H_2O)_2$] to [TiO_4]. The later shares adjacent O vertices with $P1O_4$ to produce [$(Ti_2O_4)_2(PO_4)_2$] SBU with 4-member window. Figure 6 shows that the arrangement of SBUs remains essentially the same after dehydration. As **π-TiP_0**, the anhydrous phase also shows a 3D-framework but with titanium atoms both in tetrahedral and octahedral coordination environments linked only by vertex-sharing (Figure 6).

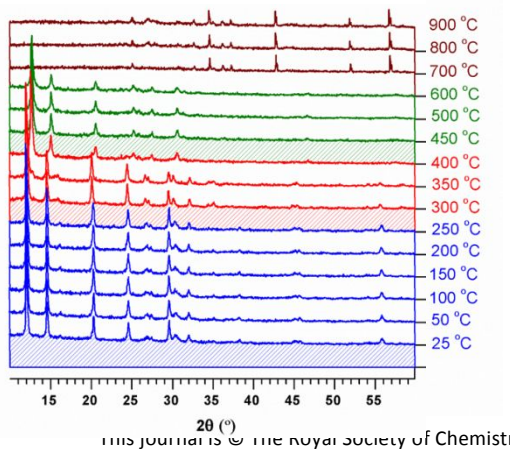

Figure 5. HT-PXRD pattern of **π-TiP_0** recorded heating up from 25 °C to 900 °C in an open air. Color codes correspond to the structural changes: blue – pristine **π-TiP_0** phase, red –partially dehydrated π-TiP, green – completely dehydrated π-TiP, brown – a mixture of TiP_2O_7 $Ti_5O_4(PO_4)_4$ phases.

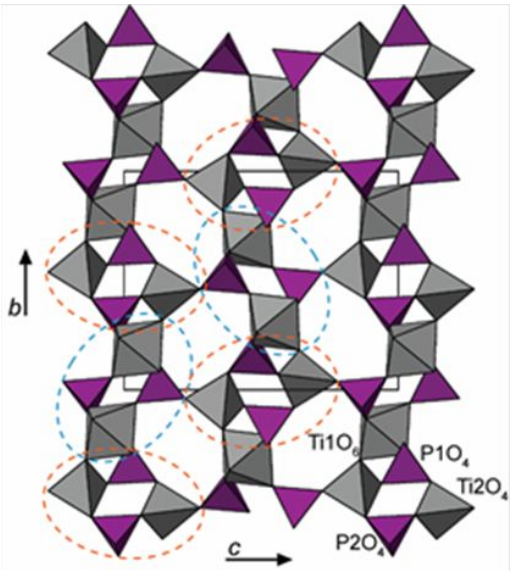

Figure 6. The projection of $Ti_2O(PO_4)_2$ structure is viewed along [001] direction. The alternating connection of the distinct SBUs types is highlighted by blue and orange dashed lines (PO_4 tetrahedra are violet and TiO_n (n = 4 or 6) are dark-grey shaded).

The anhydrous compound, π-$Ti_2O(PO_4)_2$, rehydrates partially after cooling down from 500 °C to room temperature to give $Ti_2O(PO_4)_2{\cdot}1.5H_2O$, with a loss of 7.71 wt % (Figure S6) in agreement with the calculated value 8.0 wt %. Furthermore, the powder diffraction pattern strongly resembles that of as-synthesized π-TiP although with larger diffraction peaks broadening (Figure S7).

Electrochemical measurements

As protonated phosphate species remained in the isolated **π-TiP** compound, as revealed by ^{31}P MAS-NMR, proton conductivities were measured for the as-synthesized compound (**π-TiP_0**) as well as for samples after several cycles of washing (denoted as **π-TiP_x**, where x stands for 4 or 10) in order to evaluate the effect of these species on proton conductivity. The temperature dependence of the proton conductivity for the series is displayed in Figure 7 (Figure S8 shows corresponding Nyquist plots). Proton conductivity values at 90 °C and 95%-RH, and activation energies, determined from Arrhenius plots, are given in Table 1. The structure and composition remains unperturbed after proton conductivity measurements as was revealed by PXRD and thermogravimetric analyses of the solids, therefore, those materials are completely stable under applied impedance measurement conditions (Figure S9).

Interestingly, the as-synthesized solid, **π-TiP_0**, exhibits a high proton conductivity, σ ~$1.3{\cdot}10^{-3}$ S·cm^{-1} at 90 °C and 95%-RH, which drops down to $3.4{\cdot}10^{-4}$ at 75%-RH (Figure S10), as usually observed for water-mediated proton conductors.[41] In addition, the partially rehydrated 500 °C-heated sample showed the lowest proton conductivity, which might be attributed to changes in particles size and/or surface groups activity involved in proton transfer processes. Since the progressive reduction in proton conductivity with the number of washing cycles was observed (see data for **π-TiP_4** and **π-TiP_10** in Figure 7), significant extrinsic contribution to the proton conductivity mechanism is inferred.

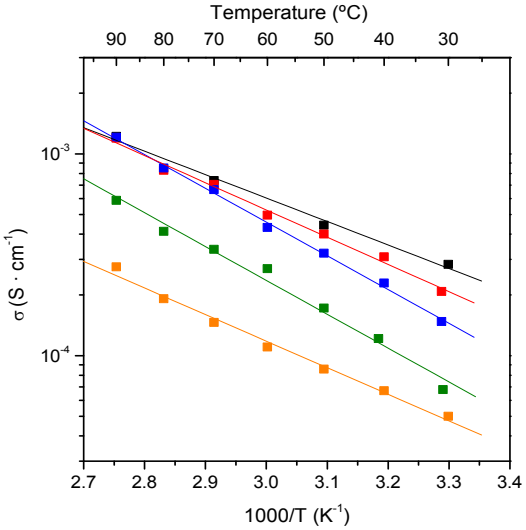

Figure 7. Plot of measured proton conductivity as function of temperature (Arrhenius plot) for **π-TiP_x** series at 95%-RH: as-synthetized **π-TiP_0** (black), water-leached **π-TiP_4** (red) and **π-TiP_10** (green), partially rehydrated **π-TiP_10** (orange) and **H_3PO_4@π-TiP_10** (blue).

In order to identify possible ion migration pathways, it has been employed the bond-valence (BV) method[42] reformulated into a force field[43] combining a local Morse-type potential (attractive term) together with a screened Coulomb potential (repulsive term). Using this energy function, the bond-site energy of the mobile ion can be predicted throughout the unit cell. Hence, a bond valence energy landscape (BVELs) can be composed enabling visual inspection of ion migration pathways outlined by energy isosurfaces of certain threshold energy (E_{th}). The latter is understood as an energy at which isosurfaces start to percolate the unit cell in at least one dimension and corresponds to an approximate value for activation energy for ion migration (E_m). We used DFT-based structural model as input because only that held accurate information about positions of H-atoms in a comparison to one that was established from present Rietveld refinements. The dense grid of points separated at 0.1 Å was used to construct projections of probe H-atoms trajectory along *a*, *b* and *c* directions of unit cell. It was found that percolation energy was considerably higher for *a*-axis of 3.50 eV and discarded for further analysis. A view on the BVLE projection onto (*bc*) plane affords an idea of 2-dimensional proton conduction of **π-TiP_0**. Calculated pathway (Figure 8) is continuous along [001] and uniform at the segment H2···H1···H3, while the bottleneck point is located at near the midpoint of H3···H4 distance. Estimated percolation energy is of 0.84 eV, indicating a vehicular-type proton transfer mechanism.[44] However, this value is higher than the determined by impedance spectroscopy, < 0.4 eV for all samples, value that is characteristic of a Grotthuss-type mechanism. This disagreement between both theoretical and experimental results could be due to several reasons. Thus, the density functional theory does not take into

accounts finite temperature effects, while the experimental conditions are different of *T*= 0 K and, and specially, the extrinsic contribution to the conductivity. Therefore, more accurate molecular dynamics studies in a bulk and on surfaces are desirable to compare with currently reported activation energies.

Table 1. ^{31}P MAS-NMR spectroscopy percentage of surface protonated phosphate species (H_3PO_4, $H_2PO_4^-$, HPO_4^{2-}), proton conductivity values (90 °C and 95%-RH) and activation energies for selected **π-TiP** derivatives.

Sample	% (H_3PO_4, $H_2PO_4^-$, HPO_4^{2-}) / PO_4^{3-}	σ×10^{-3} (S cm^{-1})	E_a (eV)
π-TiP_0	53.78	1.220	0.23
π-TiP_4	39.29	1.200	0.26
π-TiP_10	33.01	0.587	0.33
H_3PO_4@π-TiP_10	34.52	1.210	0.33

In order to evaluate the possible extrinsic contribution, ^{31}P MAS-NMR data were collected. Besides the intrinsic bands of π-TiP[36], other characteristic bands correspond to H_3PO_4 (0 ppm), $H_2PO_4^-$ (−4 to −8 ppm), and HPO_4^- (−1 to −19 ppm) species[45,46], are also observed (Table S8). As detailed in Table 1, the total contribution of these species with respect to the total PO_4^{3-} content, decreases with the growing number of washing cycles, leading to a reduction in the proton conductivity values. In a contrast to latter, the treatment with H_3PO_4 solution at room temperature (Figure 9, Tables 1 and S8) recover conductivities to the maximum value of ~10^{-3} S·cm^{-1}, which is close to the initial proton conductivity ($1.2\cdot10^{-3}$ S·cm^{-1}). This observation points to a dominant extrinsic type of proton conductivity in these materials. Comparable conductivity values were reported for the mixed-valance 3D-titanium hydrogen phosphate $Ti^{III}Ti^{IV}(HPO_4)_4$ with an intrinsic conductivity of $1.2\cdot10^{-3}$ S·cm^{-1} at 90 °C and 95% RH.[47]

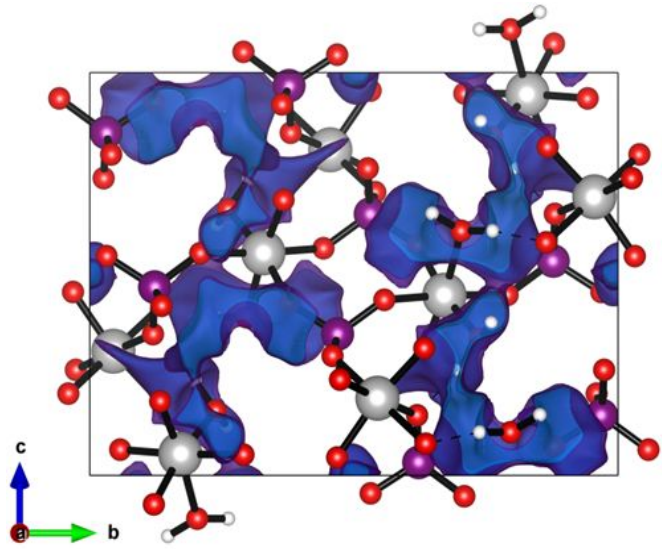

Figure 8. Projection of bond valence energy landscape calculated for onto (*bc*) plane. Darker colours are assigned for inner isosurface levels (> 0.7 eV) while the lighter hues indicate the outer levels (< 0.65 eV).

CS/π-TiP-*W* composite membranes

In the next step CS-based composite membranes (**CS/π-TiP_*W***) with 5 and 10% (w/w) loads of **π-TiP** were prepared to evaluate the effect of impregnation of **π-TiP_0** with H_3PO_4 as a proton conductivity enhancing guest molecule. SEM-EDX analysis (Figure 10) confirmed a homogeneous dispersion of the solid in both prepared membranes, with a molar ratio Ti:P = 1 as it was found in the pristine solid. The SEM images also suggest that the fibrous **π-TiP** particles seem to adopt a specific arrangement, which can be related with the growth of peak intensities of certain reflections in the XRD patterns (Figure S11) of composite membranes. This fact is likely due to specific interphase interaction of **π-TiP** with the organic host matrix. Furthermore, the **π-TiP** solid remains unaltered after soaking in an acetic acid solution (Figure S11). Thermal stability of all composite membranes is uniformly described by the same pathway (Figure S12) consists of three conventional steps. The first one takes place in a range 20–200 °C, and attributed to the dehydration of the composite membranes. The next steep losses of weight between 200 and 300 °C correspond to the oxidative degradation of chitosan as previously described in ref.48.

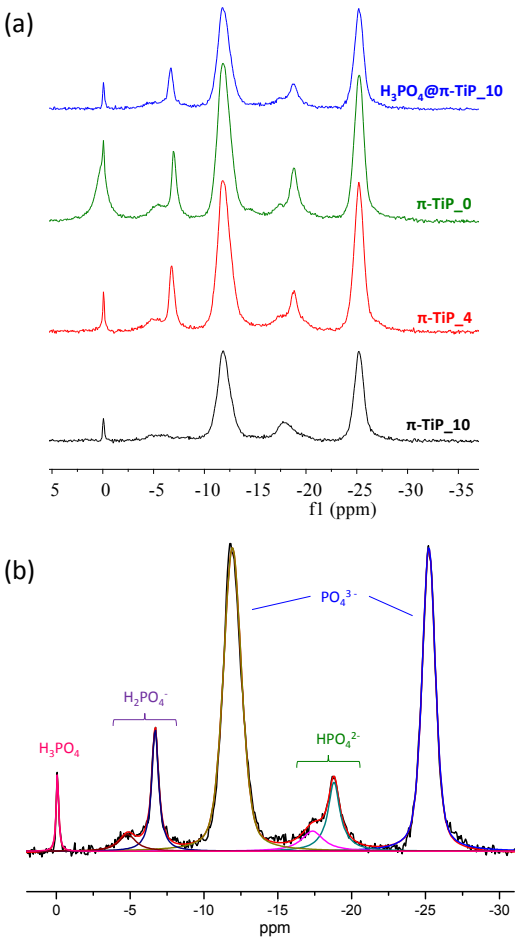

Figure 9. (a) ^{31}P MAS-NMR spectra of as-synthetized **π-TiP_0** (green), **π-TiP_4** (red) and **π-TiP_10** (black) and **H_3PO_4@π-TiP_10** (blue) after washing treatment. (b) Deconvoluted ^{31}P MAS-NMR spectrum showing several components assigned to $H_mPO_4^{n-}$ (n = 3−m, m≤3) identities present at **H_3PO_4@π-TiP_10**.

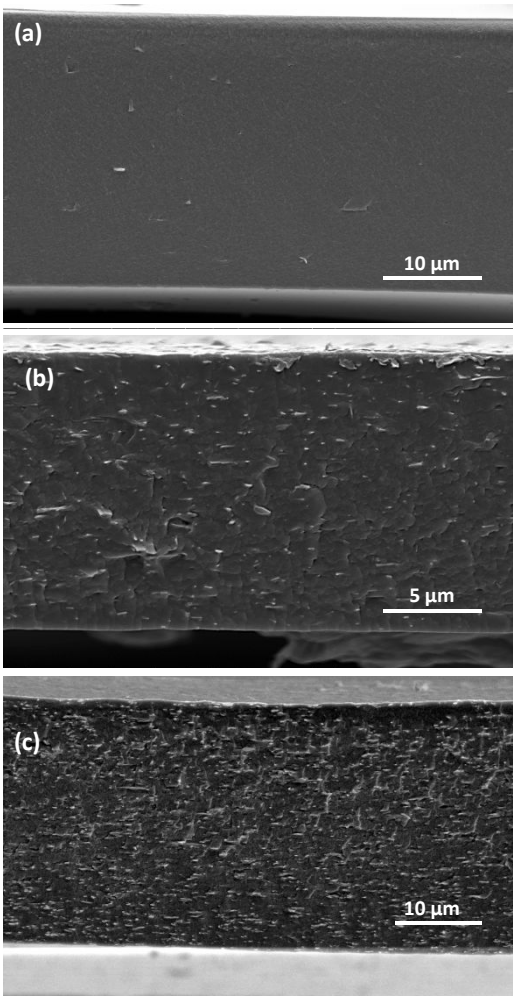

Figure 10. SEM cross-section images of (a) **CS**, (b) **CS/π-TiP-*5*** and (c) **CS/π-TiP-*10***.

The Nyquist plots are given in Figure S13, correspond to the in-situ through-plane proton conductivity measurements. As can be observed in Figure 11, Arrhenius-like plots show that **CS/π-TiP-*5*** composite membrane exhibits the best performance spanning over all temperatures of measurement, holding the score of proton conductivity of $4.5 \cdot 10^{-3}$ S·cm^{-1} (80 °C, 95% RH), that exceeds 1.8-fold the parameter for a bare **CS** membrane. This value is close to those reported for other titanium-containing CS composite membranes having similar degree of deacetylation (~ 82%)[49], but lower than other highly deacetylated (> 90%) CS composite membranes, functionalized with metal oxide and/or carbon nanotubes.[50] However, **π-TiP** loaded up with H_3PO_4 to 10 w/w % does not lead to scaling up of proton conductivity relatively to **CS** membrane parameter (Table 2).

Derived from Arrhenius plots activation energy values suggest that the proton transport is promoted mainly through a vehicle mechanism (E_a > 0.53 eV)[51], that has been also assumed earlier from BVELs calculations. This behavior could be correlated with the observed high water uptake, in particular, for **CS/π-TiP-*5*** composite membrane (137.0%), which is almost twice as much as bare CS membrane (70.8%). The incorporation of H_3PO_4-impregnated **π-TiP** into CS matrix increases water uptake in the membrane, which may promote vehicle-type mechanism for proton-transport via generation of H_2O–H_3PO_4 clusters, as well as enabling new proton-transfer pathways.[52] However, heavily loaded composite membranes, like in a case of **CS/π-TiP-*10***, are less hygroscopic and concomitantly lower conductive (Table 2), as it has been already observed for other CS-based composite membranes.[48]

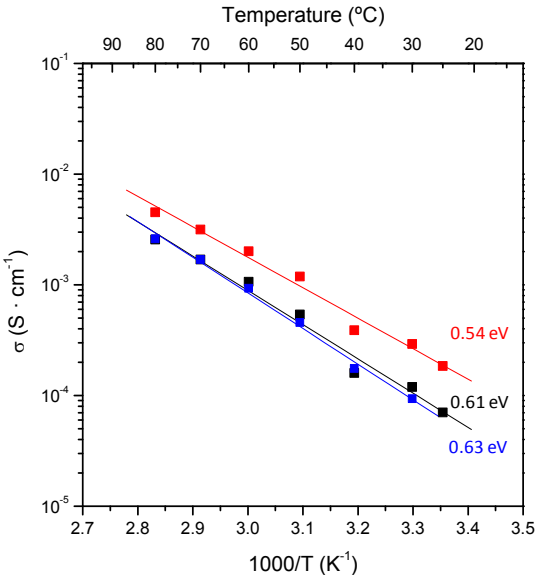

Figure 11. Arrhenius-like dependence plot of the conductivity (95% RH) of the membranes versus inverse temperature: **CS** (black), **CS/π-TiP-*5*** (red) and **CS/π-TiP-*10*** (blue).

Table 2. Calculated water uptake and proton conductivity of **CS**, **CS/π-TiP-*5*** and **CS/π-TiP-*10*** membranes at 80 °C and 95% RH.

Membrane	Water uptake (%)	Thickness (mm)	σ×10^{-3} (S cm^{-1})	Activation Energy (Ea, eV)
CS	70.89	0.06	2.57	0.54
CS/π-TiP-*5*	137.04	0.04	4.52	0.61
CS/π-TiP-*10*	90.16	0.07	2.61	0.63

Experimental Section

General instrumentation

Phosphoric acid (H_3PO_4, 85% w/w) and titanium tetrachloride ($TiCl_4$) were purchased from VWR Prolabo and Sigma-Aldrich, respectively, and used without the further purification. Differential thermal analysis (DTA) and thermogravimetric analysis (TGA) data were recorded on an SDTQ600 analyzer from TA Instruments. The temperature varied from room temperature to 900 °C at a heating rate of 10 °C·min^{-1}. Measurements were carried out on samples in open platinum crucibles under a flow of air of 10 °C·min^{-1}.

Synthesis of π-TiP_x

For the preparation of the a- synthesized solid (**π-TiP_0**), a 4 M H_3PO_4 solution was mixed with a 2 M $TiCl_4$ at a volume ratio of 2:1 in a 100 mL stainless steel Teflon-lined vessel, sealed and dwelled for 8 days 190 °C at autogenous pressure. The resultant precipitate was filtered and left to dry at 50 °C in open air. Different fractions of the solid were stirred in deionized water and centrifuged several times, and finally dried in open air [hereafter denotes as **π-TiP_x**, where x – the number of washing/centrifugation cycles (4, 6, 8 and 10)].

Synthesis of H_3PO_4@π-TiP_10.

350 mg of **π-TiP_10** compound was suspended in 0.1 M H_3PO_4 solution (20 mL) stirred at a room temperature for 2 h, filtered and dried in air.

Preparation of the membranes

Chitosan (CS) [Sigma-Aldrich, deacetylation degree (DD) 75-85%] and **CS/π-TiP-*W*** (*W* = mass percentage) containing 5 and 10% of π-TiP were prepared according to the reference method.[53] As an example, the preparation of **CS/π-TiP-*5*** composite membrane is described in detail. CS (1.5 g) was dissolved in an acetic acid aqueous solution (2% v/v, 50 mL) in a flask under magnetic stirring at 80 °C for 12 hours. In parallel, the π-TiP compound (0.22 mmol, 75 mg) was dispersed in an acetic acid aqueous solution (2% v/v, 25 mL) under magnetic stirring for 30 min at room temperature and alternating with ultrasonic treatment (30 min) for three consecutive cycles to yield the solution equivalent to concentration of CS in acetic acid. The resulting solutions were mixed and magnetically stirred (1 h) and sonicated (1 h) for three consecutive cycles to obtain a homogenous suspension. After degasification, the membrane was cast onto a glass plate using a doctor blade (BYK Instrument) and dried at a room temperature. The membranes were immersed in a 2.0 M H_2SO_4 solution for 24 h for completing cross-linking. The films were extensively washed in deionized water to remove the residual H_2SO_4 and dried at a room temperature in an open air.

Structural analysis

Synchrotron-radiation powder X-ray diffraction (SRPXRD) data were collected using beamline 11-BM-B (λ =0.457904 Å) under cryogenic conditions (*T* = 100 K) at the Advanced Photon Source (APS), Argonne National Laboratory (Lemont, IL, USA). Powder X-ray thermodiffraction (HT-PXRD) studies were carried out on a sample loaded in an Anton Paar HTK 1200N oven-chamber under static air. Data were collected on a Mavlern-PANalytical X'Pert Pro diffractometer, using monochromatic Cu Kα1 radiation (λ = 1.54056 Å) and the X'Celerator position-sensitive detector. Each powder pattern was recorded in the 10–80° range (2θ) at intervals of 50 °C from room temperature up to 900 °C, with a step of 0.026° and a counting time of 0.424 s per step. All measurements were carried out with a heating rate of 10 °C·min^{-1} and a delay time of 10 min to ensure thermal stabilization. The structural determination of π-TiP heated at 500 °C was carried out by simulated annealing procedure implemented in the program EXPO2014 and using the crystal structure of the anhydrous ρ-TiP polymorph as initial model.[54] Rietveld refinements[55] of the crystals against the powder diffraction data were performed with the Buker AXS TOPAS v4.2 software.

Electron microscopy studies

The transmission electron microscopy (TEM) investigations were performed on a JEOL JEM-2100F TEM operating at an accelerating voltage of 200 kV and equipped with a field emission gun and an ultra-high-resolution pole-piece that provide a point-resolution better than 0.19 nm. This microscope is also equipped with scanning transmission electron microscope (STEM) control unit (Gatan), energy dispersive X-ray (EDX) detector (Oxford Instruments, silicon drift detector (SDD) 80 mm^2), CCD camera (14-bit Gatan Orius SC600), and bright-field (BF) and high-angle annular dark-field (HAADF) detectors (JEOL). This microscope was used for high-resolution TEM (HRTEM), selected area electron diffraction (SAED), STEM-EDX analysis (line-scan and area mapping) and electron diffraction (ED) tomography. Fine powder of the sample was dispersed in ethanol, sonicated and sprayed on a lacey-carbon-coated copper grid (200 mesh, EM science), and then allowed to air dry. Afterwards, the dried grid was mounted onto a single-tilt holder. Acquiring, processing and analysis of all micrographs were performed using Gatan Digital Micrograph software. Quantitative analyses were done using INCA Microanalysis Suite software version 4.15. The serial electron diffraction dataset was processed using ADT3D software.

Solid-State ^{31}P MAS-NMR spectroscopy study

Spectra were recorded at RT in an AVANCE III HD 600 (Bruker AXS) spectrometer using a triple resonance CP-MAS probe of 3.2 mm at a spinning rate of 15 kHz. The magnetic field was 14.1 T corresponding to a ^{31}P resonance frequency of 242.92 MHz. The ^{31}P chemical shifts were referenced to H_3PO_4. ^{31}P MAS-NMR spectra were recorded with a 3 ms contact time and 5 s delay with ^{1}H decoupling (^{31}P CP-MAS and ^{31}P Hpdec with spinal decoupling sequence 64 for P) and summing up 64 scans. The deconvolution of ^{31}P MAS-NMR spectrum were carried out using the DMFIT program.[56]

Characterization of Chitosan composite membranes (CS/π-TiP-*W*)

Chitosan and **CS/π-TiP-*W*** composite membranes were characterized by PXRD, thermogravimetric analysis under N_2 and SEM-EDX (Helios Nanolab 650 and an energy dispersive X-ray spectrometer X-Max Oxford). Water uptake of the membranes was determined by measuring the weight variation before and after hydration. The membranes were firstly dried at 60 °C for 24 hours and then weighed (dry weigh, W_{dry}). Afterwards, the membranes were immersed in deionized water for 24 h, wiped with a tissue paper to remove any excess water on the film surface and quickly weighted again (wet weight, W_{wet}). The water uptake was calculated by the following equation:

$$Water\ uptake\ (\%) = [(W_{wet} - W_{dry})/W_{dry}] \times 100 \qquad (1)$$

Proton conductivity measurements

Impedance measurements of **π-TiP_x** solids were carried out on cylindrical pellets (~5 mm diameter; ~0.9 – 1.1 mm thickness) obtained by pressing of ca. 30 – 40 mg of a substance at 250 MPa for 1 min. Pellets were placed between porous carbon (Sigracet, GDL 10 BB, Pt-free) or, alternatively, silver electrodes were loaded on opposite bases of the pellets by painting with a silver conducting paste (Sigma-Aldrich). The sample cells were placed inside a temperature and humidity-controlled chamber (Espec SH-222).

The impedance data were collected using a potentiostat Autolab (AUT88029, PGSTAT302N) equipped with a Frequency Response Analyser (FRA 32M) module over the frequency range from 20 Hz to 1 MHz with an applied voltage of 0.35 V (**π-TiP_x**); or 0.1 Hz and 1 MHz, with an applied voltage of 0.01 V and a bias of 0 V (**CS** and **CS/π-TiP-*W*** membranes). To equilibrate the water content, pellets and composite membranes were initially preheated (0.2 °C min^{-1}) from 30 to 90 °C at relative humidity (RH) values of 95, 90, 85, 80 and 75% RH, for **π-TiP_0** solid, and 95% RH for rest of probed materials. Impedance spectra were recorded during cooling using stabilization times of 5 h (pellets) or 10 h (membranes). Water condensation on the sample was suppressed by reducing the relative humidity before decreasing the temperature. For all compounds, the total pellet resistances (R_T) were obtained from the analysis of spectra using ZView2 program, which were normalized to the geometry of the samples to calculate the conductivity values using the following equation: $\sigma = L\cdot(R_T S)^{-1}$, where L is the thickness of the pellets and S is the surface area of the electrodes. In-plane proton conductivity (two-probes method) for composite membranes was determined from the expression $\sigma_{\parallel} = L\cdot(R_T S)^{-1}$; being *L* the distance between the two electrodes and *S* the cross-section area of the membrane.

Periodic boundary phase calculations

Periodic boundary density functional theory (PB-DFT) calculations were carried out using the projector-augmented wave method, as implemented in the Vienna *ab initio* simulation package (VASP).[57,58] Initial coordinates of atoms in the unit cell were taken from PXRD-refined crystal structure and used for further optimizations. Generalized gradient approximation of DFT in Perdew-Becke-Ernzerhof revised for solids (PBEsol) parametrization was applied to account for electron exchange and correlation. Empirical correction for dispersion forces to the energies was accounted using Tkachenko-Scheffler approach.[59] Full details of computational procedures are given in the Supporting Information.

Conclusions

Fibrous titanium phosphate π-$Ti_2O(PO_4)_2\cdot 2H_2O$ (**π-TiP_0**), obtained under mild hydrothermal conditions, crystallizes in the monoclinic system, space group $P2_1/c$, in a contrast to previously reported ρ-$Ti_2O(PO_4)_2\cdot 2H_2O$ (ρ-TiP). 3D framework of **π-TiP_0** is built with TiO_6 and $TiO_4(H_2O)_2$ octahedra, bridged by the orthophosphate groups, assembled into the SBUs arrange into alternating fashion similar to ρ-TiP. Planar packing imperfections, observed by HRTEM and causing anisotropic SRPXRD peaks broadening, are likely responsible for stacking faults altering the stacking sequence of the planes (00−1) in as-synthesized crystalline nanorod material. This solid can be fully dehydrated to the $Ti_2O(PO_4)$ phase at 500 °C though the complex thermally induced framework rebuilt, partially reducing titanium coordination environment from octahedral to tetrahedral. The solid ultimately decompose into a mixture of TiP_2O_7 and $Ti_5O_4(PO_4)_4$, as confirmed by Rietveld analysis. Studies focused on surface modification of **π-TiP_0** indicate that this solid exhibits a high extrinsic vehicle-type proton conductivity ($1.3\cdot10^{-3}$ $S\cdot cm^{-1}$, at 90 °C and 95% RH) due to presence of superficially protonated phosphate/water clusters, as revealed by ^{31}P MAS-NMR. Preliminary studies on Chitosan-based composite membranes (**CS/π-TiP_*W***) suggest that doping the CS matrix with π-TiP (5 w/w %) results in 1.8-fold rise of the proton conductivity in comparison to bare CS membrane at 80 °C and 95% RH.

Author Contributions

The manuscript was written through contributions of all authors. All authors have given approval to the final version of the manuscript.

Conflicts of interest

There are no conflicts to declare.

Acknowledgements

This work has been supported by Ministerio de Ciencia, Innovación y Universidades and Ministerio de Economía, Industria y Competitividad from Spain (MAT2016-78155-C2-1-R, MAT2016-77648-R and PID2019-110249RB-I00), Junta de Andalucía (FQM-113) research project and Principado de Asturias–FICYT-FEDER (IDI/2018/000170).

Use of the Advanced Photon Source at Argonne National Laboratory was supported by the U. S. Department of Energy, Office of Science, Office of Basic Energy Sciences, under Contract No. DE-AC02-06CH11357. Artem A. Babaryk would like to thank Prof. Santiago García-Granda (SYSTAM Group) at Department of Physical and Analytical Chemistry for the SRPXRD data (APS 11 BM-B “Mail-In” program, under proposal no. GUP-65338). Prof. José Manuel Recio (MALTA-Consolider Team) is acknowledged for providing computational facilities at the University of Oviedo. The authors thank Prof. José R. García and S. Khainakov of the Oviedo University, Spain, for his appreciated contribution. L. dos Santos-Gómez thanks the Ministerio de Ciencia, Innovación y Universidades for her Juan de la Cierva Formación grant (FJC2018-036746-I), M. Bazaga-García thanks Junta de Andalucía for her Postdoc PAIDI grant and R. M. P. Colodrero thanks UMA Research Plan for her financial support.

Notes and references

Corresponding Author

*L. dos Santos-Gómez and *Artem A. Babaryk, Department of Physical and Analytical Chemistry, Avda. Julián Clavería 8, Campus de El Cristo, Oviedo University-CINN, 33006-Oviedo, Spain; ldsg@uniovi.es; artem.babaryk@gmail.com

*M. Bazaga-García, Departamento de Química Inorgánica, Cristalografía y Mineralogía, Campus de Teatinos s/n, Universidad de Málaga, 29071-Málaga, Spain; m.bazaga@uma.es

1 Y. Zhao, Y. Mao, W. Zhang, Y. Tang and P. Wang, *Int. J. Hydrog. Energy*, 2020, **45**, 23174–23200.
2 Y. Wang, D. F. Ruiz Diaz, K. S. Chen, Z. Wang and X. Cordobes Adroher, *Mater. Today,* 2020, **32**, 178–203.
3 M. B. Karimi, F. Mohammadi and K. Hooshyari, *Int. J. Hydrog. Energy,* 2019, **44**, 28919–28938.
4 N. A. H. Rosli, K. S. Loh, W. Y. Wong, R. M. Yunus, T. K. Lee, A. Ahmad and S. T. Chong, *Int. J. Mol. Sci.,* 2020, **21**, 632.
5 S. I. Lee, K. H. Yoon, M. Song, H. Peng, K. A. Page, C. L. Soles and D. Y. Yoon, *Chem. Mater.,* 2012, **24**, 115–122.
6 S. Subianto, M. K. Mistry, N. R. Choudhury, N. K. Dutta and R. Knout, *ACS Appl. Mater. Interfaces,* 2009, **1**, 1173–1182.
7 C. H. Park, C. H. Lee, M. D. Guiver and Y. M. Lee, *Prog. Polym. Sci.,* 2011, **36**, 1443-1498.
8 L. Vilciauskas, S. J. Paddison and K. D. Kreuer, *J. Phys. Chem. A,* 2009, **113**, 9193–9201.
9 H. Steininger, M. Schuster, K. D. Kreuer, A. Kaltbeitzel, B. Bingoel, W. H. Meyer, S. Schauff, G. Brunklaus, J. Maier and H. W. Spiess, *Phys. Chem. Chem. Phys.,* 2007, **9**, 1764–1773.
10 T. Dippel, J. C. Lassegues, K. D. Kreuer and D. Rodriguez, *Solid State Ion.,* 1993, **61**, 41–46.
11 Q. Qin, Q. W. Tang, B. L. He, H. Y. Chen, S. S. Yuan and X. Wang, *J. Appl. Polym. Sci.,* 2014, **131**, 40622.
12 Z. J. Cai, R. Li, X. L. Xu, G. G. Sun, X. P. Zhuang, Y. Liu and B. Cheng, *Polymer,* 2018, **156**, 179–185.
13 J. C. Dang, L. P. Zhao, J. Zhang, J. D. Liu and J. T. Wang, *J. Membr. Sci.,* 2018, **545**, 88–98.
14 S. Horike, D. Umeyama, M. Inukai, T. Itakura and S. Kitagawa, *J. Am. Chem. Soc.,* 2012, **134**, 7612−7615.
15 S. Tao, L. Zhai, A. D. Dinga Wonanke, M. A. Addicoat, Q. Jiang and D. Jiang, *Nat. Commun.,* 2020, **11**, 1981.
16 A. Pal, S. C. Pal, K. Otsubo, D. W. Lim, S. Chand, H. Kitagawa and M. C. Das, *Chem. Eur. J.,* 2020, **26**, 4607–4612.
17 D. W. Kang, M. Kang and C. S. Hong, *J. Mater. Chem. A,* 2020, **8**, 7474–7494.
18 Y. H. Yin, Z. Li, X. Yang, L. Cao, C. B. Wang, B. Zhang, H. Wu and Z. Y. Jiang, *J. Power Sources,* 2016, **332**, 265–273.
19 L. A. Diaz, G. C. Abuin and H. R. Corti, *J. Electrochem. Soc.,* 2016, **163**, F485–F491.
20 X. Sun, J. H. Song, H. Q. Ren, X. Y. Liu, X. W. Qu, Y. Feng, Z. Q. Jiang and H. L. Ding, *Electrochim. Acta,* 2020, **331**, 135235.
21 V. G. Ponomareva, K. A. Kovalenko, A. P. Chupakhin, D. N. Dybtsev, E. S. Shutova and V. P. Fedin, *J. Am. Chem. Soc.,* 2012, **134**, 15640−15643.
22 T. Kasuga, M. Nakano and M. Nogami, *Adv. Mater.* 2002, **14**, 1490–1492.
23 E. Bakangura, L. Wu, L. Ge, Z. Yang and T. Xu, *Prog. Polum. Sci.*, 2016, **57**, 103-152.
24 G. Alberti, M. Casciola, A. Donnadio, P. Piaggio, M. Pica and M. Sisani, *Solid State Ion*., 2005, **176**, 2893-2898.
25 M. Taddei, A. Donnadio, F. Costantino, R. Vivani and M. Casciola, *Inorg. Chem*., 2013, **52**, 12131-12139.
26 M. Taddei, R. Vivani and F. Costantino, *Dalton Trans*., 2013, **42**, 9671-9678.
27 B. Mosby, A. Díaz, V. I. Bakhmutov and A. Clearfield, *ACS Appl. Mater. Interfaces*, 2013, **6**, 585-592.
28 F. Bauer and M. Willert-Porada, *J. Power Sources*, 2005, **145**, 101-107.
29 Y. Bereznitski, M. Jaroniec, A. I. Bortun, D. M. Poojary and A. Clearfield, *J. Colloid Interface Sci.,* 1997, **191**, 442–448.
30 Y. Zhu, G. Hasegawa, K. Kanamori, T. Kiyomura, H. Kurata, K. Hayashi and K. Nakanishi, *CrystEngComm.*, 2017, **19**, 4551–4560.
31 Y. Zhu, G. Hasegawa, K. Kanamori and K. Nakanishi, *Inorg. Chem. Front.*, 2018, **5**, 1397–1404.
32 J. García-Glez, Z. Amghouz, I. da Silva, C. O. Ania, J. B. Parra, C. Trobajo and S. García-Granda, *Chem. Commun.,* 2017, **53**, 2249–2251.
33 M. Yada, Y. Inoue, A. Sakamoto, T. Torikai and T. Watari, *ACS Appl. Mater. Interfaces*, 2014, **6**, 7695−7704.
34 B. Cai, N. Jiang, P. Tan, Y. Hou, Y. Li and L. Zhang, *RSC Adv.,* 2019, **9**, 41311−41318.
35 I. García, C. Trobajo, Z. Amghouz, R. Díaz-Velasco, M. Alonso-Guervos, R. Mendoza-Meroño, M. Mauvezín-Quevedo and A. Adawy, 2021, *submitted for publication*.
36 A. I. Bortun, S. A. Khainakov, L. N. Bortun, D. M. Poojary, J. Rodriguez, J. R. Garcia and A. Clearfield, *Chem. Mater.,* 1997, **9**, 1805–1811.
37 A. A. Coelho, *J. Appl. Cryst*., 2003, **36**, 86–95.
38 C. Serre, N. Guillou and G. Ferey, *J. Mater. Chem*., 1999, **9**, 1185–1189.
39 M. Järvinen, *J. Appl. Cryst.,* 1993, **26**, 525–531.
40 A. Boultif and D. Louer, *J. Appl. Cryst*., 2004, **37**, 724–731.
41 K. Otake, K. Otsubo, T. Komatsu, S. Dekura, J. M. Taylor, R. Ikeda, K. Sugimoto, A. Fujiwara, C. P. Chou, A. W. Sakti, Y. Nishimura, H. Nakai and H. Kitagawa, *Nat. Commun.,* 2020, **11**, 843.
42 I. D. Brown, *Chem. Rev.,* 2009, **109**, 6858–6919.
43 S. Adams and R. P. Rao, *Phys. Status Solidi A-Appl. Mater. Sci.,* 2011, **208**, 1746–1753
44 N. Agmon, *Chem. Phys. Lett*., 1995, **244**, 456–462.
45 C.-Y. Chen, F.-R. Lo, H.-M. Ka and K.-H. Lii, *Chem. Commun.,* 2000, 1061–1062.
46 A. I. Bortun, E. Jáimez, R. Llavona, J. R. García and J. Rodríguez, J. *Mater. Res. Bull.,* 1995, **30**, 413–420.
47 P. G. M. Mileo, T. Kundu, R. Semino, V. Benoit, N. Steunou, P. L. Llewellyn, C. Serre, G. Maurin and S. Devautour-Vinot, *Chem. Mater.,* 2017, **29**, 7263–7271.
48 G. Liu, W. C. Tsen, F. Hu, F. Zhong, J. Wang, H. Liu, S. Wen, G. Zheng, C. Qin and C. Gong, *Int. J. Hydrog. Energy,* 2020, **45**, 29212–29221.
49 A.-C. Humelnicu, P. Samoila, M. Asandulesa, C. Cojocaru, A. Bele, A. T. Marinoiu, A. Sacca and V. Harabagiu, *Polymers*, 2020, **12**, 1125-1142.
50 G. Liu, W.-C. Tsen, F. Hu, F. Zhong, J. Wang, H. Liu, S. Wen, G. Zheng, C. Qin and C. Gong, *Int. J. Hydrogen Energy*, 2020, **45**, 29212-29221.
51 E. Prokhorov, G. Luna-Bárcenas, J. B. González-Campos, Y. Kovalenko, Z. Y. García-Carvajal and J. Mota-Morales, *Electrochim. Acta,* 2016, **215**, 600–608.
52 J. Wang, H. Zhang, X. Yang, S. Jiang, W. Lv, Z. Jiang and S. Z. Qiao, *Adv. Funct. Mater*., 2011, **21**, 971–978.
53 X. Y. Dong, J. J. Li, Z. Han, P. G. Duan, L. K. Li and S. Q. Zang, *J. Mater. Chem., A* 2017, **5**, 3464–3474.
54 A. Altomare, C. Cuocci, C. Giacovazzo, A. Moliterni, R. Rizzi, N. Corriero and A. Falcicchio, *J. Appl. Cryst.,* 2013, **46**, 1231–1235.
55 H. M. Rietveld, *J. Appl. Cryst*., 1969, **2**, 65–71.
56 D. Massiot, F. Fayon, M. Capron, I. King, S. Le Calve, B. Alonso, J-O. Durand, B. Bujoli, Z. Gan and G. Hoatson, *Magn. Reson. Chem.,* 2002, **40**, 70–76.
57 G. Kresse and J. Furthmuller, *Phys. Rev. B.,* 1996, **54**, 11169−11186.
58 G. Kresse and J. Furthmuller, *Comput. Mater. Sci.,* 1996, **6**, 15−50.
59 A. Tkatchenko and M. Scheffler, *Phys. Rev. Lett.,* 2009, **102**, 073005.

TOC

The structure of elusive π-$Ti_2O(PO_4)_2$×$2H_2O$ (π-TiP) was successfully determined by the SR-PXRD method and co-characterized by HRTEM, ^{31}P SS-NMR and HT-PXRD. The proton conductivity of chitosan/π-TiP membranes reaches 4.5×10^{-3} S cm^{-1} at 80 °C and 95%-RH.